A modified phase diversity wavefront sensor with a diffraction grating

Luo Qun(罗 群)[a)b)c)†], Huang Lin-Hai(黄林海)[b)c)], Gu Nai-Ting(顾乃庭)[b)c)], and Rao Chang-Hui(饶长辉)[b)c)]

[a)] *College of Opto-Electronics Science and Engineering, National University of Defense Technology, Changsha* 410073, *China*

[b)] *The Laboratory on Adaptive Optics, Institute of Optics and Electronics, Chinese Academy of Sciences, Chengdu* 610209, *China*

[c)] *The Key Laboratory on Adaptive Optics, Chinese Academy of Sciences, Chengdu* 610209, *China*

(Received 31 December 2011; revised manuscript received 18 January 2012)

Phase diversity wavefront sensor is one of the useful tools to estimate the wavefront aberration, and it is often used as a wavefront sensor in adaptive optics system. However, the performance of the traditional phase diversity wavefront sensor is limited by the accuracy and dynamic ranges of the intensity distribution at focus and defocus positions of the CCD camera. In this paper, a modified phase diversity wavefront sensor based on a diffraction grating is proposed to improve the ability to measure the wavefront aberration with larger amplitude and higher spatial frequency. The basic principle and the optics construction of the proposed method are also described in detail. The noise propagation property of the proposed method is also analysed by using the numerical simulation method, and comparison between the diffraction grating phase diversity wavefront sensor and the traditional phase diversity wavefront sensor is also made. The simulation results show that the diffraction grating phase diversity wavefront sensor can obviously improve the ability to measure the wavefront aberration, especially the wavefront aberration with larger amplitude and higher spatial frequency.

Keywords: phase diversity wavefront sensor, diffraction grating, aberration, signal-to-noise ratio

PACS: 42.15.Fr, 42.25.Fx, 42.30.Rx, 42.40.Pa **DOI:** 10.1088/1674-1056/21/9/094201

1. Introduction

Wavefront sensor (WFS) is one of the key parts in adaptive optics system, and its measurement accuracy determines the ability to control the wavefront.[1,2] During the past decades, many kinds of wavefront sensors have been proposed, such as Hartmann–Shack WFS, curvature WFS, pyramid WFS,[3] interferometry, and phase diversity wavefront sensor (PDWFS). Comparatively, the PDWFS has a simple and compact optical configuration. In addition, lower environment requirement and good measurement accuracy make it become an attractive candidate as the WFS in adaptive optics. With the development of computer technology, the speed of the PDWFS restructing algorithm has been improved greatly, and the PDWFS should be implemented successfully in many domains, especially in solar adaptive optics.[4−13]

In 1979, the theory of the PD wavefront sensing technology was proposed first by Gonsalves and Hidlaw.[4] Since then, a lot of investigators have devoted to increasing the speed of PD algorithm and expanding the scope of application. Paxman and Fienup[5] applied PD to co-phasing a multi-aperture system in 1988. In 1999 and 2000, Blanchard and Greenaway,[6] and Blanchard *et al.*[7] described a novel PD wavefront sensor comprising a distorted diffraction grating and a single camera, so that a series of focused and defocused images could be collected by one CCD camera at the same time. In 2004, Campbell *et al.*[8] introduced a quadratically distorted diffraction grating which can be used to simultaneously image multiple object planes onto a single CCD camera, and then they used a pair of images of the wavefront plane to reconstruct the unknown wavefront aberration.

PD is an image-based wavefront sensing technology for estimating the unknown wavefront phase from focused and defocused images. The measurement accuracy is limited by many factors, which include system aberrations, stray light, sample rate and detector noise and so on. When PDWFS works under the monochromatic point source, the wavefront aberrations, especially the high-spatial-frequency components, could cause the energy spread in the focal and

†Corresponding author. E-mail: littlepuppet_luo@sina.com

© 2012 Chinese Physical Society and IOP Publishing Ltd

defocused planes. The dispersed intensity distribution contains the wavefront phase information with high-spatial-frequency, and the detecting noise of CCD camera will degrade the measurement accuracy of the intensity distribution at focus and defocus positions. Finally, the high-spatial-frequency component is hard to reconstruct due to detection noise, and the capability of the traditional phase diversity wavefront sensor (T-PDWFS) is limited.

In this paper, we develop a novel optical structure of PDWFS, in which a grating is used to improve the measurement accuracy, and we name it phase diversity wavefront sensor based on a diffraction grating (G-PDWFS). The diffraction grating is placed in front of the imaging lens, and it splits the incidence beam into a number of beamlets with different light energies. Finally, the different diffraction order spots enter into the CCD cameras and are imaged onto the focal plane and defocus plane, respectively. The image stitching technology is employed to calculate the intensity distribution on the focus and defocus planes with two or more diffraction spots. The calculated spots contain more information in the lower light level part of original image, which is submersed in noise. In this case, the random wavefront phase can be reconstructed from the new images, and the measurement accuracy can be improved.

2. Theory

2.1. Traditional phase diversity wavefront sensor

The optical structure for a phase diversity system is shown in Fig. 1.

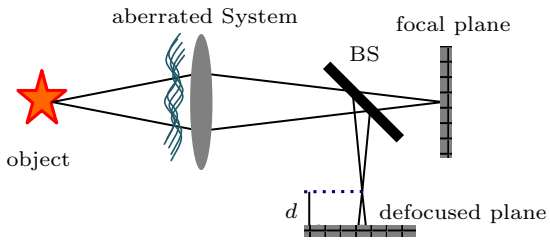


Fig. 1. (colour online) Optical layout for a phase diversity system.

In Fig. 1, an object is imaged to the focus plane and defocus plane by an imaging lens and a beam splitter (BS), and they are captured by two CCD cameras. The defocus distance of the defocus plane is d. When an object is illuminated with spatially incoherent monochromatic light and imaged by a linear shift-invariant system, the image formation process will be approximated by the following Fourier transform:[4]

$$\begin{aligned} I'_{\rm f}(\boldsymbol{w}) &= |h_{\rm f}(\boldsymbol{w})|^2 = |\Im\{p(\boldsymbol{r})[\exp {\rm i}\Phi(\boldsymbol{r})]\}|^2, \\ I'_{\rm d}(\boldsymbol{w}) &= |h_{\rm d}(\boldsymbol{w})|^2 \\ &= |\Im\{p(\boldsymbol{r})\exp\{{\rm i}[\Phi(\boldsymbol{r})+\Phi_{\rm d}(\boldsymbol{r})]\}\}|^2, \end{aligned} \quad (1)$$

where $\boldsymbol{r}$ and $\boldsymbol{w}$ are the pupil plane and image plane Cartesian coordinate respectively; $p(\boldsymbol{r})$ is the amplitude of generalized pupil function; $\Phi(\boldsymbol{r})$ is the wavefront aberration that is to be measured; $\Phi_{\rm d}$ is the defocused phase function introduced by known defocused amount; $\Im\{\}$ is Fourier transform; $h_{\rm f}$ and $h_{\rm d}$ are the impulse response functions of the focal plane and defocused plane respectively; $I'_{\rm f}$ and $I'_{\rm d}$ are the intensity distributions of the focal spot and defocused spot respectively.

The noise at each detector element is modeled as an additive and identical distributed random variable. The intensity distributions detected by two CCD cameras can be represented by

$$\begin{aligned} I_{\rm f} &= I'_{\rm f}(\boldsymbol{w}) + n(\boldsymbol{w}), \\ I_{\rm d} &= I'_{\rm d}(\boldsymbol{w}) + n(\boldsymbol{w}), \end{aligned} \quad (2)$$

where $n(\boldsymbol{w})$ is the additive detector noise, $I_{\rm f}$ and $I_{\rm d}$ are intensity distributions including detector noise.

The PD restructing algorithm is used to match the intensities which are computed from a model estimate of system to the detected images. If the additive Guassian noise model is adopted, the unknown wavefront aberration Φ can be retrieved by minimizing the cost function[5]

$$\begin{aligned} E = \sum_{\boldsymbol{w}} \big[&|I_{\rm f} - |\Im\{p(\exp {\rm i}\Phi)\}|^2|^2 \\ &+|I_{\rm d} - |\Im\{p\exp {\rm i}[(\Phi+\Phi_{\rm d})]\}|^2|^2\big]. \end{aligned} \quad (3)$$

In this paper, we adopt PD restructing algorithm which was presented by Baba and Nutoh[14] in 2001.

2.2. Grating phase diversity wavefront sensor

In this section, we will present the modification made into the T-PDWFS, and it is the PDWFS based on diffraction gratings. The optical layout is shown in Fig. 2. The diffraction grating divides the incidence beam into a number of beamlets, and they have the same wavefront phases and the different light intensities. Then these beamlets are imaged onto the focus plane and the defocus plane by an imaging lens, and a set of diffraction spots, which have different intensity amplitudes but have the same intensity distribution, is

formed. Finally, these images on the two planes (i.e. focus and defocus plane) are captured by two CCD cameras simultaneously.

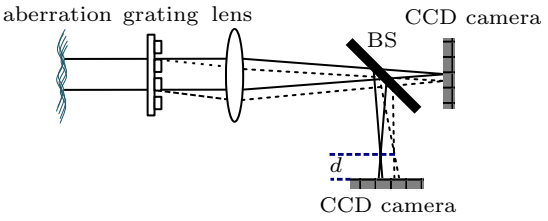


Fig. 2. Optical layout for a grating phase diversity system.

In the following, we take a one-dimensional diffraction grating as an example to explain the focused image and defocused image of intensity distribution. For a diffraction grating, its transmission function can be written as

$$t(\boldsymbol{r}) = \Big[\frac{1}{2} + \frac{m}{2}\cos(2\pi f_0 x)\Big]\mathrm{rect}\Big(\frac{x}{2L}\Big)\mathrm{rect}\Big(\frac{y}{2L}\Big), \quad (4)$$

where L is the length of grating; $\mathrm{rect}(x/2L)\mathrm{rect}(y/2L)$ is a two-dimensional rectangular function with a pupil function of grating; f_0 is the grating-spatial-frequency; m is the peak-to-valley ratio of transmission function. If a collimated monochromatic beam with a unit amplitude and the circular aperture input are perpendicular to the diffraction grating surface, its complex amplitude function can be represented as

$$U(\boldsymbol{r}) = \mathrm{circ}(\boldsymbol{r}/a)\exp[\mathrm{i}\Phi(\boldsymbol{r})], \quad (5)$$

where $\Phi(\boldsymbol{r})$ is the wavefront phase distribution, $\mathrm{circ}(\boldsymbol{r}/a)$ is the wavefront amplitude distribution and a is the radius of the aperture. In this paper, the wave amplitude is a circular function and it is assumed to be unity within the pupil and zero elsewhere.

According to Eqs. (4) and (5), we can obtain the complex amplitude distribution in the back surface of the diffraction grating, and it is shown as

$$\begin{aligned} U_{\mathrm{t}}(\boldsymbol{r}) &= U(\boldsymbol{r})t(\boldsymbol{r}) \\ &= \Big[\frac{1}{2} + \frac{m}{2}\cos(2\pi f_0 x)\Big]\mathrm{circ}\Big(\frac{\boldsymbol{r}}{a}\Big) \\ &\quad \times \exp[\mathrm{i}\Phi(\boldsymbol{r})]. \end{aligned} \quad (6)$$

On the focal plane, the Fraunhofer diffraction pattern of grating is given by

$$U_{\mathrm{g}}(\boldsymbol{\rho}) = \Im\{U_{\mathrm{t}}(\boldsymbol{r})\}, \quad (7)$$

where $\boldsymbol{\rho}$ is the image plane polar coordinates. If the incidence beam is an ideal aberration-free wavefront ($\Phi(\boldsymbol{r}) = 0$), the distribution of circular function is as follows:

$$\begin{aligned} h(\boldsymbol{\rho}) &= \Im\{\mathrm{circ}(\frac{\boldsymbol{r}}{a})\} \\ &= \exp\Big[\mathrm{i}\Big(kf + \frac{k\boldsymbol{\rho}^2}{2f}\Big)\Big] \\ &\quad \times \frac{\pi a^2}{\mathrm{i}\lambda f}\Big[\frac{2J_1(ka\boldsymbol{\rho}/f)}{ka\boldsymbol{\rho}/f}\Big], \end{aligned} \quad (8)$$

and a factor, $G(f_u, f_v)$, about diffraction order is

$$\begin{aligned} G(f_u, f_v) &= \Im\{\frac{1}{2} + \frac{m}{2}\cos(2\pi f_0 x)\} \\ &= \frac{1}{2}\delta(f_u, f_v) + \frac{m}{4}\delta(f_u + f_0, f_v) \\ &\quad + \frac{m}{4}\delta(f_u - f_0, f_v), \end{aligned} \quad (9)$$

where $f_u = u/\lambda f$, $f_v = v/\lambda f$, with (u, v) being a position parameter in the rectangular coordinate system. According to the convolution theorem and Eqs. (1), (2) and (7)–(9), the complex amplitude distribution on the focal plane can be expressed as

$$\begin{aligned} U_{\mathrm{g}}(\boldsymbol{w}) &= \frac{1}{2}h(u, v) + \frac{m}{4}h(u + \lambda f f_0, v) \\ &\quad + \frac{m}{4}h(u - \lambda f f_0, v). \end{aligned} \quad (10)$$

According to Eq. (10), the intensity distribution can be calculated as

$$\begin{aligned} I_{\mathrm{g}}(u, v) &= |U_{\mathrm{g}}(u, v)|^2 \approx \frac{1}{4}|h(u, v)|^2 \\ &\quad + \frac{m^2}{16}|h(u - \lambda f f_0, v)|^2 \\ &\quad + \frac{m^2}{16}|h(u + \lambda f f_0, v)|^2. \end{aligned} \quad (11)$$

From Eq. (11), the focused image and defocused image about the diffraction grating contain the 0th and ±1st order diffraction spots, and the shapes of intensity distributions of these spots are the same, while the position of spot centre and the intensity of spot are different from spot to spot. The ratio of the 0th order diffraction spot peak value to ±1st order just depends on the grating parameter, and it can be represented as $\eta = 4/m^2$.

The imaging process of G-PDWFS is simulated based on Eq. (11), and the focused image and defocused image are shown in Fig. 3. The central and more brightly spot is the 0th order diffraction spot, denoted by $I_{\mathrm{g}0}$, and the bilateral spots are the ±1 order diffraction spots. We add the ±1 order diffraction spots together, then multiplied by $\eta/2$, and the result is denoted by $I_{\mathrm{g}1}$. Comparing the $I_{\mathrm{g}0}$ and $I_{\mathrm{g}1}$, there are some pixels in the central part of the $I_{\mathrm{g}0}$ which

are saturated, so these pixels cannot exactly express the intensity distribution on the focal and defocused planes. However, the pixels in the surrounding part of the I_{g0} are clearer than I_{g1}, and these pixels contain many details of intensity distribution. We use the corresponding pixels in I_{g1} to replace the saturation pixels in I_{g0}, and the new spot image is denoted by I_g. Obviously, the new intensity distribution I_g not only exactly expresses the intensity distribution, but also contains much more detailed information. In fact, wavefront aberrations of many applications include not only low-spatial-frequency components such as astigmatism, defocusing, coma, and spherical aberration, but also some high-spatial-frequency components, which information is included mainly in the surrounding area of the focus spot and embedded in noise and cannot be detected by T-PDWFS. Based on the grating, the dynamic range of CCD camera is expanded. Using the new intensity distributions in PD restructing algorithm to estimate the wavefront aberration, the measurement accuracy of G-PDWFS will be enhanced.

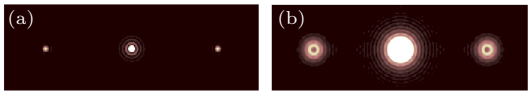


Fig. 3. (colour online) G-PDWFS images without aberration: (a) focused image, (b) defocused image.

3. Numerical simulation

3.1. Numerical simulation of T-PDWFS

In what follows, a series of numerical simulations was run to compare the measurement accuracy of G-PDWFS with that of T-PDWFS. In this section, we study the measurement accuracy of T-PDWFS on the assumption of the images without detector noise. After that, we analyse the effects on measurement accuracy of detector noise with various levels. We take the following parameters for numerical simulation.

1) The size of the discrete matrix in the pupil plane has 512 rows and 512 columns. The sample space of aberration beam is 128 rows and 128 columns in a circular field. The focused image and defocused image both have 512×512 pixels.

2) For the wavefront aberration test, a random wavefront aberration, Φ_0, is generated by using the 1th–65th order terms of Zernike polynomial as shown in Fig. 4(a). The coefficients of Zernike polynomial are shown in Fig. 4(b). The detected aberration Φ_0 is 0.111λ root-mean-square (RMS), and is 1λ peak-to-valley (PV).

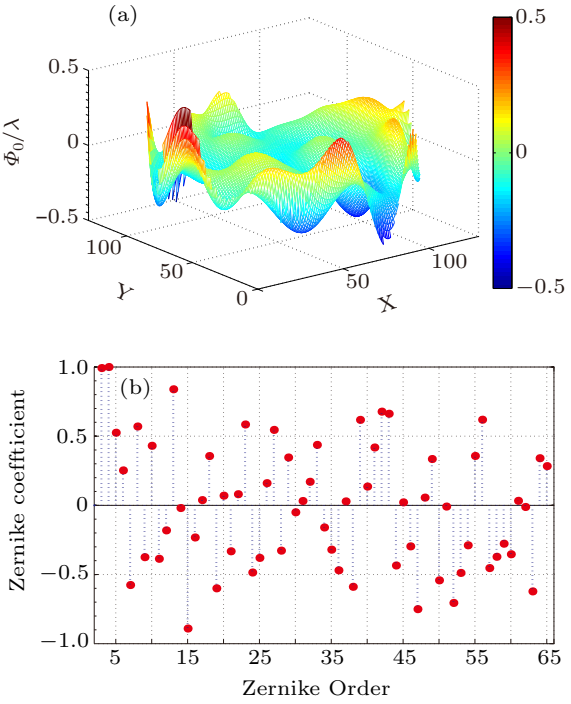


Fig. 4. (colour online) Detected aberration used in this study, denoted by Φ_0. (a) Φ_0: aberration is 0.111λ RMS and 1λ PV, (b) coefficients of Zernike polynomial.

3) In this paper, the defocused mode is chosen to be a diversity function, and the relationship between the known defocusing amount d and PV of defocused aberration in wavefront is given by

$$\Phi_{\mathrm{d}}^{\mathrm{PV}} = d/8\lambda(F^{\#})^2, \tag{12}$$

where d is the distance of defocus, λ is the wavelength, and $F^{\#}$ is the image space f-number which is 30 for this simulation. In our simulation, we use 0.25λ RMS of quadratic focus diversity to generate the defocused image.

In the case of no detector noise, the simulated images on the focus and defocus planes are shown in Figs. 5(a) and 5(b) respectively, and their peak values are all normalized to 1. In Fig. 5, only the central regions (128 pixel × 128 pixel) are drawn.

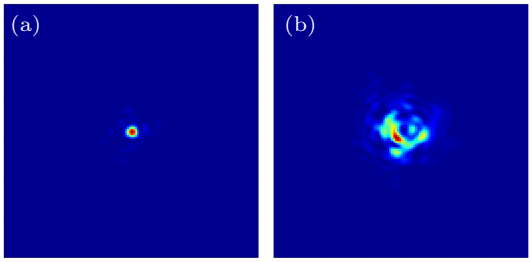


Fig. 5. (colour online) Example of the intensity distribution images of T-PDWFS, without detector noise: (a) focused image, (b) defocused image.

Using these images by the PD reconstruction algorithm to estimate the detected wavefront aberration Φ_0, as a result, the reconstructed aberration Φ is 0.110λ RMS, and is 0.987λ PV. The measurement accuracy is evaluated by computing the RMSE (root-mean-squared error) between the reconstructed wavefront aberration Φ and wavefront aberration Φ_0. The RMSE is computed by

$$\begin{aligned} \text{RMSE} &= \sqrt{\frac{1}{N^2}\sum_{i,j}(\Phi-\Phi_0)^2} \\ &= \sqrt{\frac{1}{N^2}\sum_{i,j}(\Delta\Phi)_{ij}^2}, \end{aligned} \tag{13}$$

where N^2 is the number of image pixels, $\Delta\Phi$ is the residual error between Φ and Φ_0. In this simulation, the RMSE is $2.23\times10^{-3}\lambda$ and the $\Delta\Phi$ is $3.76\times10^{-2}\lambda$ PV. It is shown that the reconstructed wavefront aberration, which is estimated by PDWFS without detector noise, is fairly close to the systemic static aberration. This result shows that this wavefront sensing technique is a high-accuracy technique.

However, the detector noise cannot be avoided, and the noisy intensity depends on the performance of CCD camera. When the noise is present, the intensity distribution information, which is used in PD restructing algorithm, is not exactly collected, so that the measurement accuracy of PDWFS will be degraded. In our simulation, we will consider the influence of CCD camera noise. Firstly, we assume that the dominant noise mechanism is detector reading noise, so the intensity distribution images can be given by an additive, zero-mean Gaussian random variable. Secondly, we define the signal-to-noise ratio (SNR) as a peak-to-noise ratio of light intensity distribution. Finally, the peak intensity in each image is set to be 80% of 16 bits to simulate analog-to-digital conversion. A series of digital simulations is made to compare the measurement accuracies of T-PDWFS for various levels of SNR.

The detected wavefront aberration Φ_0 used for this study is shown in Fig. 4(a). The 10 sets of independent detector noises, with the SNR ranging from 10000 to 10, are generated. Figure 6 shows the RMSE of residual wavefront $\Delta\Phi$ versus SNR. From the result, the measurement accuracy of T-PDWFS is degraded as the SNR decreases from 10000 to 10. For high SNR (weak noisy intensity in the pixel), the T-PDWFS achieves a high accuracy in estimation. When the SNR decreases to 2000, the ratio of the RMSE to the Φ RMS is more than 10%. For low SNR, some weak optical information cannot be exactly recorded due to the fact that detector noise distribution will submerge into light intensity distribution. In this case, unrealistic values are reconstructed and consequently the PD restructing algorithm fails to accurately measure.

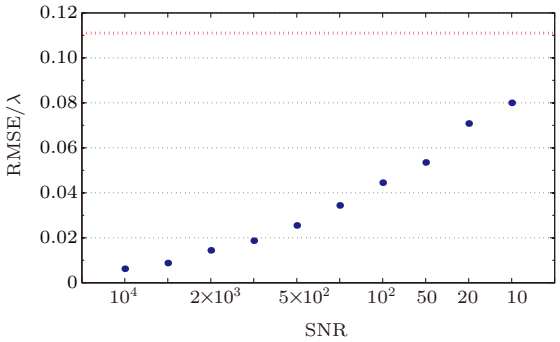


Fig. 6. (colour online) RMSE of residual error versus SNR. Φ_0 is 0.11λ RMS.

3.2. Numerical simulation of G-PDWFS

In this section, we will compare the G-PDWFS with T-PDWFS on estimating the detected wavefront aberration by numerical simulation under the same SNR. The detected wavefront aberration Φ_0 is also the aberration which is shown in Fig. 4(a). The simulation parameters are the same as those in Subsection 3.2. The ratio of the 0th order diffraction spot peak value to the $\pm$1st order is 64 for this simulation, and the transmission function of one-dimension diffraction grating is

$$t = 1/2 + (1/8)\cos(2\pi x/3). \tag{14}$$

Based on the principle of G-PDWFS, images are simulated to test the accuracy under four conditions: (I) when the peak intensity in each image is set to be 80% of 16 bits to simulate analog-to-digital conversion, (II) when the peak pixel of the $\pm$1st order diffraction spots does not reach the saturation value, (III) when an additive, zero-mean Gaussian noise is added, and (IV) when the SNR is defined as a ratio of light-intensity distribution peak to noise. When the SNR of CCD camera is 200, focused image and defocused image which are normalized by the peak intensity in each image, and three-dimensional images are shown in Figs. 7(a) and 7(b). According to the image processing method which is described in Subsection 2.2, new intensity distribution images can be obtained, and the central regions of these normalized images are shown in Figs. 7(c) and 7(d). To compare with this new technique, we generate the focused and defocused images of T-PDWFS at the same detector SNR, and the images are shown in Figs. 7(e) and 7(f).

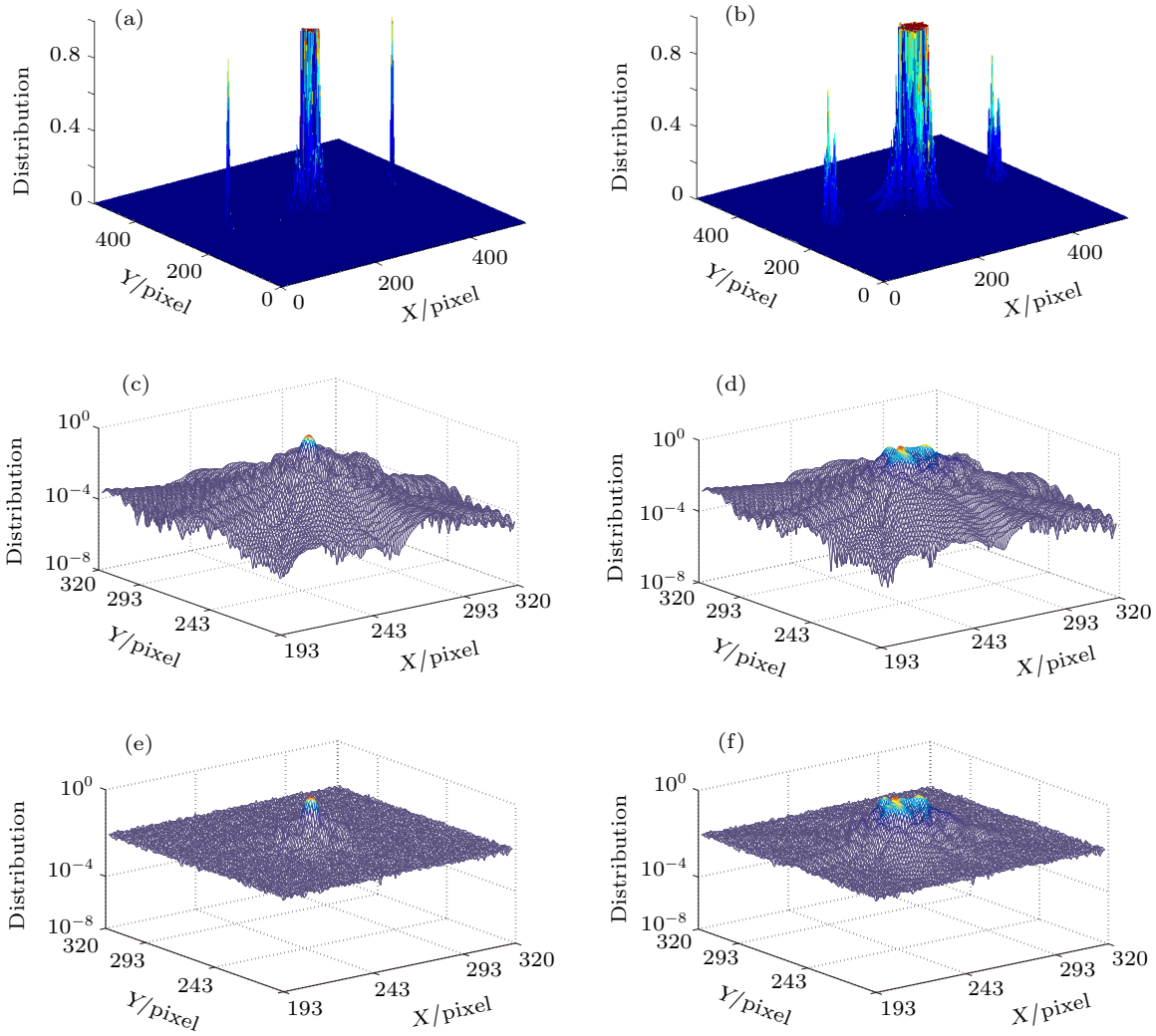


Fig. 7. (colour online) Intensity distribution images: (a) focused image on CCD camera of G-PDWFS, (b) defocused image on CCD camera of G-PDWFS, (c) intensity distribution on focal plane, (d) intensity distribution on defocused plane, (e) focused image of T-PDWFS, (f) defocused image of T-PDWFS.

Figure 8 shows the reconstruction wavefront aberrations, when the SNR of the CCD camera is 200, residual aberrations for detected aberration (Fig. 4(a), for 0.111λ RMS, and 1λ PV) with respect to G-PDWFS and T-PDWFS. Figure 8(a) shows the reconstruction wavefront aberration by G-PDWFS, denoted by $\Phi_{\rm G}$, 0.109λ RMS, and 0.971λ PV. Figure 8(b) exhibits the residual aberration between $\Phi_{\rm G}$ and Φ_0, which is denoted by $\Delta\Phi_{\rm G}$, $6.98\times10^{-3}\lambda$ RMSE and 0.132λ PV. Figure 8(c) displays the reconstruction wavefront aberration by T-PDWFS, denoted by $\Phi_{\rm T}$, $9.23\times10^{-2}\lambda$ RMS and 0.593λ PV. Figure 8(d) indicates the residual aberration between $\Phi_{\rm T}$ and Φ_0, denoted by $\Delta\Phi_{\rm T}$, $3.44^{-2}\lambda$ RMSE and 0.657λ PV. Figure 8(e) reveals the Zernike coefficients of $\Phi_{\rm G}$ and Φ_0. Figure 8(f) presents the Zernike coefficients of $\Phi_{\rm T}$ and Φ_0. Figure 8(g) demonstrates the differences between the Zernike coefficients of Φ_0 and reconstruction wavefront aberrations.

In this section, we generate 4 sets of focused and defocused images with SNR decreasing from 500 to 50, and the results of simulation with respect to wavefront aberration estimation are shown in Table 1.

From the simulation results in Fig. 8 and Table 1, when the SNRs are the same, in comparison with T-PDWFS, the reconstruction wavefront aberration $\Phi_{\rm G}$ of G-PDWFS is much more close to the detected aberration Φ_0, and the RMSE is much smaller. It is shown in Figs. 8(e) and 8(f) that for the high-spatial-frequency Zernike polynomial, the measurement accuracy of G-PDWFS is much better than that of T-PDWFS. As expected, the wavefront measurement accuracy is improved with diffraction grating, especially for the high-spatial-frequency components in the reconstruction wavefront aberration.

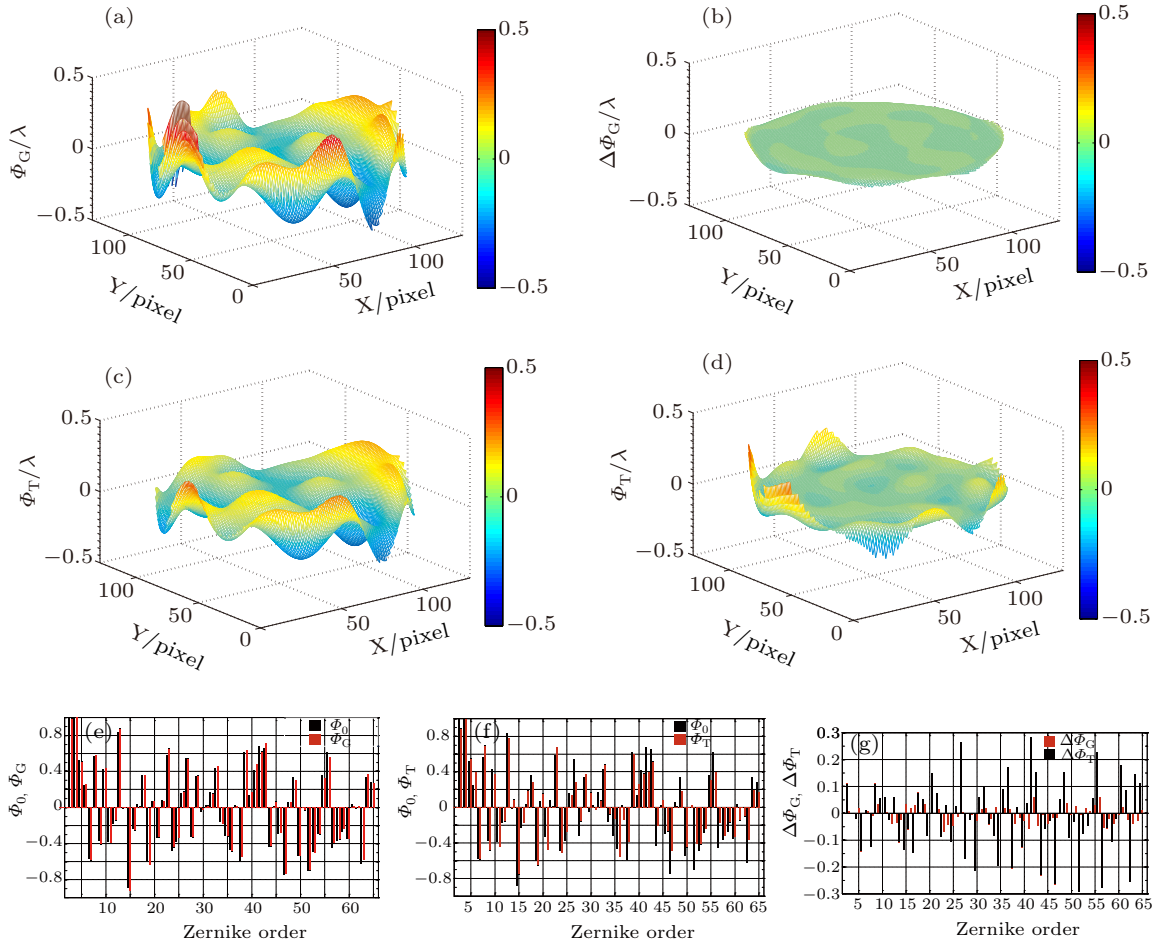


Fig. 8. (colour online) Results of numerical simulation, when the SNR is 200: (a) the reconstruction wavefront aberration by G-PDWFS, (b) the residual aberration between $\Phi_{\rm G}$ and Φ_0, (c) the reconstruction wavefront aberration by T-PDWFS, (d) the residual aberration between $\Phi_{\rm T}$ and Φ_0, (e) the Zernike coefficients of $\Phi_{\rm G}$ and Φ_0, (f) the Zernike coefficients of $\Phi_{\rm T}$ and Φ_0, (g) Zernike coefficients of $\Delta\Phi_{\rm G}$ and $\Delta\Phi_{\rm T}$.

Table 1. Simulation results of G-PDWFS and T-PDWFS with several SNRs.

SNR	G-PDWFS				T-PDWFS			
	$\Phi_{\rm G}$		$\Delta\Phi_{\rm G}$		$\Phi_{\rm G}$		$\Delta\Phi_{\rm G}$	
	RMS (λ)	PV (λ)	RMS (λ)	PV (λ)	RMS (λ)	PV (λ)	RMS (λ)	PV (λ)
500	0.110	0.993	5.92×10^{-3}	0.103	9.82×10^{-2}	0.700	2.55×10^{-2}	0.516
200	0.109	0.971	6.98×10^{-3}	0.132	9.23×10^{-2}	0.593	3.44×10^{-2}	0.657
100	0.108	0.941	9.23×10^{-3}	0.178	8.54×10^{-2}	0.496	4.45×10^{-2}	0.771
50	0.105	0.916	1.32×10^{-2}	0.240	7.84×10^{-2}	0.423	5.35×10^{-2}	0.830

4. Discussion and conclusion

In the present paper, a novel PDWFS method is proposed to improve measurement accuracy. We describe the basic principle of the proposed method, and also illustrate in detail the optics configuration with a diffraction grating. Numerical simulation is performed to validate the accuracy of the proposed method and its noise error propagation property. In addition, a comparison between the proposed method and the traditional PDWFS is also simulated numerically.

From the results, the proposed method has a good noise error propagation property, and better measurement accuracy is obtained by using it as a WFS, especially for the wavefront aberration with larger amplitude and higher spatial frequency.

References

[1] Bobcock H W 1953 *Publ. Astron. Soc. Pac.* **65** 229

[2] Hardy J W, Lefebvre J E and Koliopoulos C L 1997 *J. Opt. Soc. Am.* A **67** 360
[3] Wang J X, Bai F Z, Ning Y, Huang L H and Jiang W H 2011 *Acta Phys. Sin.* **60** 029501 (in Chinese)
[4] Gonsalves R A and Hidlaw R C 1979 *Proc. SPIE* **207** 32
[5] Paxman R G and Fienup J R 1988 *J. Opt. Soc. Am.* A **5** 914
[6] Blanchard P M and Greenaway A H 1999 *Appl. Opt.* **38** 6692
[7] Blanchard P M, Fisher D J, Woods S C and Greenaway A H 2000 *Appl. Opt.* **39** 6649
[8] Campbell H I, Zhang S J, Greenaway A H and Restaino S, 2004 *Opt. Lett.* **29** 2707
[9] Meimon S, Delavaquerie E and Cassaing F 2008 *Proc. SPIE* **7012** 141
[10] Luo L, Wang L and Cheng W D 2006 *Acta Phys. Sin.* **55** 6708 (in Chinese)
[11] Thomas R and Rimmele 2011 *Solar Adaptive Optics, Living Rev. Solar Phys.* **8** 2
[12] Li F and Rao C H 2012 *Acta Phys. Sin.* **61** 029502 (in Chinese)
[13] Luo Q, Huang L H, Gu N T, Li F and Rao C H 2012 *Acta Phys. Sin.* **61** 069501 (in Chinese)
[14] Baba N and Mutoh K 2001 *Appl. Opt.* **40** 544